Provided for non-commercial research and education use.
Not for reproduction, distribution or commercial use.

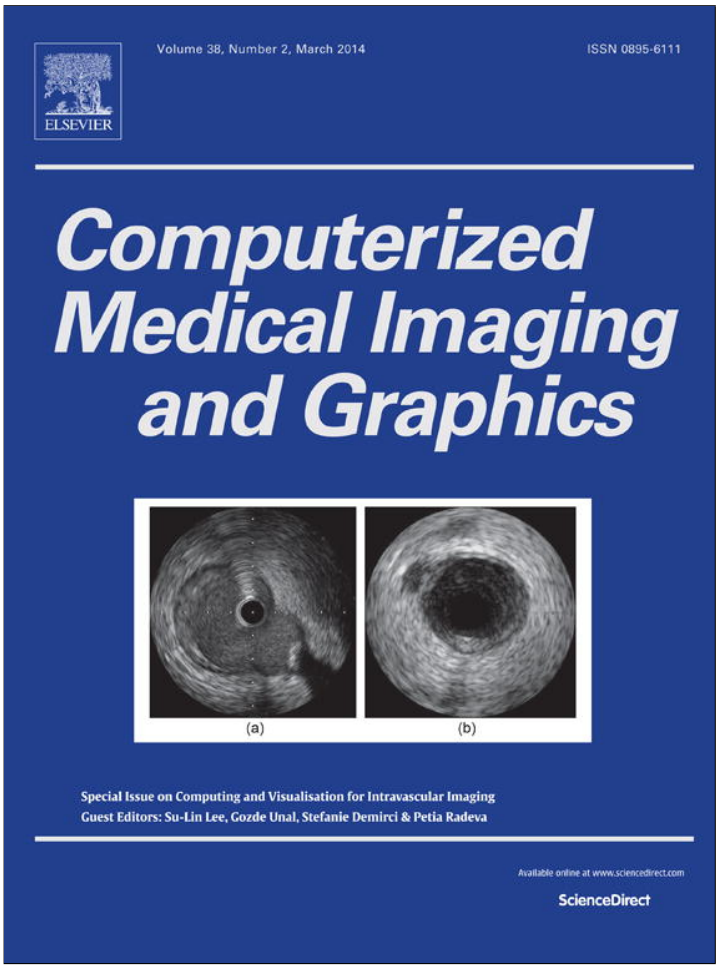

This article appeared in a journal published by Elsevier. The attached copy is furnished to the author for internal non-commercial research and education use, including for instruction at the authors institution and sharing with colleagues.

Other uses, including reproduction and distribution, or selling or licensing copies, or posting to personal, institutional or third party websites are prohibited.

In most cases authors are permitted to post their version of the article (e.g. in Word or Tex form) to their personal website or institutional repository. Authors requiring further information regarding Elsevier's archiving and manuscript policies are encouraged to visit:

http://www.elsevier.com/authorsrights

Author's personal copy

Computerized Medical Imaging and Graphics 38 (2014) 91–103

Contents lists available at ScienceDirect

Computerized Medical Imaging and Graphics

journal homepage: www.elsevier.com/locate/compmedimag

Segmentation method of intravascular ultrasound images of human coronary arteries

François Destrempes[a], Marie-Hélène Roy Cardinal[a], Louise Allard[a], Jean-Claude Tardif[b], Guy Cloutier[a,c,d,*]

[a] Laboratory of Biorheology and Medical Ultrasonics, University of Montreal Hospital Research Center (CRCHUM), Montreal, Canada
[b] Montreal Heart Institute, Montreal, Canada
[c] Department of Radiology, Radio-Oncology and Nuclear Medicine, University of Montreal, Montreal, Canada
[d] Institute of Biomedical Engineering, University of Montreal, Montreal, Canada

ARTICLE INFO

Article history:
Received 1 October 2012
Received in revised form 6 September 2013
Accepted 10 September 2013

Keywords:
Segmentation
Cardiovascular imaging
Ultrasound
Statistical analysis
Validation

ABSTRACT

The goal of this study was to show the feasibility of a 2D segmentation fast-marching method (FMM) in the context of intravascular ultrasound (IVUS) imaging of coronary arteries. The original FMM speed function combines gradient-based contour information and region information, that is the gray level probability density functions of the vessel structures, that takes into account the variability in appearance of the tissues and the lumen in IVUS images acquired at 40 MHz. Experimental results on 38 in vivo IVUS sequences yielded mean point-to-point distances between detected vessel wall boundaries and manual validation contours below 0.11 mm, and Hausdorff distances below 0.33 mm, as evaluated on 3207 images. The proposed method proved to be robust in taking into account various artifacts in ultrasound images: partial shadowing due to calcium inclusions within the plaque, side branches adjacent to the main artery to segment, the presence of a stent, injection of contrast agent or dissection, as tested on 209 images presenting such artifacts.

© 2013 Elsevier Ltd. All rights reserved.

1. Introduction

Intravascular ultrasound (IVUS) is a medical imaging modality that produces a sequence of cross-sectional frames of the vascular wall of arteries as a catheter is pulled-back inside blood vessels. It has become very useful for studying atherosclerotic diseases [1].

Various segmentation techniques have been developed for IVUS images of coronary arteries. Among methods that are based on statistics of the B-mode image, a Maximum A Posteriori (MAP) estimator was derived using Rayleigh statistics of the signal for the lumen contour segmentation [2]. A multi-surface 3D graph search using Rayleigh distributions and Chan-Vese terms is proposed in [3]. In [4], a knowledge-based approach is used to determine which level of gray corresponds statistically to the different regions of interest, i.e., the intima, plaque and lumen, in the context of the arterial wall segmentation. In [5], a non-parametric probabilistic model is integrated into a shape-driven method for the segmentation of the arterial wall. Among other probabilistic segmentation methods of the luminal borders, let us mention [6–8].

Several other techniques than the ones based on speckle statistics have also been proposed in the past five years. Edge information alone [9] or combined gray level intensity attributes [10,11] were used. Other segmentation algorithms are based on different textural features [12–15]. Gray level intensity and textural information were combined to detect the lumen boundary [6]; edge attributes were added for the external elastic membrane (EEM) [16]. In these methods, different frameworks were used to extract the vessel wall boundaries from the different image information, classifiers being the most prevalent recently [6,13,15,16]. Threshold and contour filtering [12] and binary morphological operations [14] were also proposed. Taki et al. [9] used deformable models while [10] combined them to graph search. Finally, a multi-agent segmentation [11] and a 3D parallel segmentation method [17] were investigated. Less recent techniques can be found in Section 4.

The aim of this work was to show that an adaptation of the fast-marching segmentation method developed in [18,19] for femoral artery IVUS segmentation is also powerful in the context of coronary imaging. Compared to femoral arteries [18,19], the artery wall of the coronaries presents a much more complex movement (see Fig. 1, left image). Moreover, since the IVUS images were acquired at a higher frequency (40 MHz) than in the case of femoral arteries (20 MHz), the lumen presents more speckle and hence, its appearance is more variable in the present study than in the context of [18,19] (see Fig. 1, right image). Therefore, we

* Corresponding author at: Laboratory of Biorheology and Medical Ultrasonics, University of Montreal Hospital Research Center (CRCHUM), Montreal, Canada. Tel.: +1 514 890 8000x24703; fax: +1 514 412 7505.
E-mail address: guy.cloutier@umontreal.ca (G. Cloutier).

0895-6111/$ – see front matter © 2013 Elsevier Ltd. All rights reserved.
http://dx.doi.org/10.1016/j.compmedimag.2013.09.004

Author's personal copy

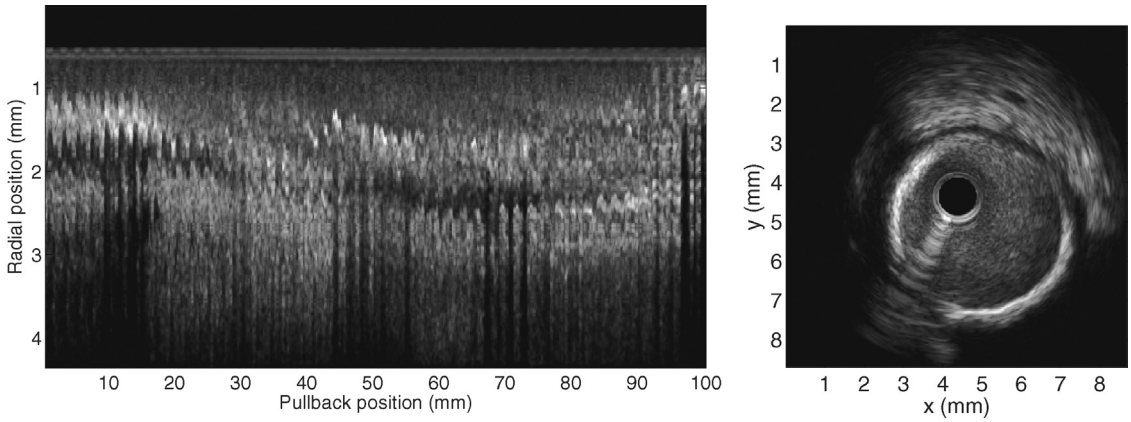

Fig. 1. Left: example of half a longitudinal cut of a pullback. Right: example of a cross-section that presents a calcified area from that in vivo sequence pullback.

considered an original modification of the speed function proposed in [18,19]. A textural gradient, defined in terms of the distribution of the gray levels in the different components of the vessel wall, was introduced in this new speed function. Moreover, mixtures of gamma probability density functions (PDFs) were used to model the gray level distribution of the log-compressed and filtered envelop of the IVUS images [20,21] that could not be modeled with Rayleigh distributions assuming uniform scattering tissues [22], as was used in our previous work. We also included a process that computes adaptive weights to calibrate the two components of the speed function to accommodate for various ranges of values coming from different image features. The vessel wall boundaries were modeled as layered contours that propagate simultaneously under that new speed function, which is based on a combination of complementary contour and region information. The multiple interfaces were propagated in the IVUS series of images after having been initially positioned using approximate manual segmentations on 2 perpendicular longitudinal views (L-views) of the 3D volume, to allow the tracking of the artery wall. This type of initialization is adapted for the segmentation of large pullbacks (several millimeters) where the vessel wall components might change across the sequence due to the heterogeneity of the image, and when adjacent cross-sections are discontinuous due to the beating heart movement for acquisitions that are not gated. This segmentation model handles contour irregularities, partial shadowing due to calcium inclusions within the plaque, side branches adjacent to the main artery to segment, the presence of a stent, injection of contrast agent or dissection as often observed for atherosclerotic coronary plaques.

2. Materials and methods

2.1. In vivo data

A total of 38 in vivo IVUS pullbacks from diseased coronary arteries was obtained from a database of Boston Scientific and clinical studies conducted at the Montreal Heart Institute. From these two sources, we segmented 20 sequences acquired with the Boston Scientific "Galaxy II" scanner, and 18 sequences with the "iLab" echograph. Ultrasound transducers at 40 MHz (mounted on catheters) were used in all cases. The IVUS cross-section image size varied between 8.2 mm and 11.4 mm. In what follows, a sequence refers to a series of IVUS images obtained by a pullback, at a constant speed, of the ultrasound catheter. The echograph "iLab" corresponds to the newest platform of Boston Scientific.

The segmentation algorithm was implemented on Matlab (version 7.04, the MathWorks, Natick, MA, USA), using some of our VC++"mex" libraries. In order to comply with Matlab memory restriction, each of the 38 original sequences was broken up into 2 or 3 smaller sequences, each one of about 1000 frames, for a total of 78 sequences totalizing 82, 848 frames.

Table 1
The eight categories of comments written by the technicians for the 1388 frames from dataset 1 that were manually segmented.

Category	Comment	Number of frames
1	None	1179
2	Dissection	20
3	Calcium	91
4	Stent	72
5	Calcium and dissection	8
6	Branching	10
7	Branching and calcium	4
8	Injection of contrast agent	4

A subset of images from each available pullback, with a step of twenty between frames, was manually segmented by experimented technicians of the Montreal IVUS Core Laboratory[1] at the Montreal Heart Institute. Overall, 4142 images were selected for the validation (82,848/20 images). Three technicians were involved in the manual segmentation of these images; the final contours were reviewed and approved by at least two technicians. The instructions given to the technicians were the following: if ever the visual perception of the image (and of the video sequence) did not allow the manual segmentation of either contour (lumen-intima or EEM-adventitia), then the image was classified as non-usable.[2] Consequently, some of the images could not be manually segmented and the total number of images that could be quantitatively analyzed (i.e., comparison of the algorithmic and manual segmentations) was 3207 (77.4% of the 4142 images, more precisely, 1388 of the 1782 "iLab" and 1819 of the 2360 "Galaxy II" frames). Thus, two datasets were used for the quantitative evaluation of the proposed segmentation method: dataset 1 consisting of the 1388 "iLab" frames (including 209 difficult frames that were nevertheless manually segmented – see Section 3.4) and dataset 2 consisting of the 1819 "Galaxy II" frames.

The technicians also wrote up in a lab book any difficulties encountered in the manual segmentation. The categories of their comments are summarized in Table 1

[1] The intraclass coefficients for interobserver variability associated with measurements of plaque and vessel volumes in this laboratory are 0.98 and 0.99, respectively [23].

[2] This instruction was imposed by the fact that a large portion of the database came from a clinical study where the area of the plaque was considered; the lumen-intima and EEM-adventitia contours are required to establish the atherosclerotic plaque area.

Author's personal copy

2.2. The fast-marching method (FMM) and its speed function

The segmentation of the two coronary artery boundaries (i.e., the lumen-intima and the EEM-adventitia boundaries) was performed with the FMM [24]. The goal of that method is to find the boundary between two regions (i.e., in the present study, two tissues) m and n by letting evolve two interfaces, one that starts within tissue m and moves toward the boundary, and the other one that starts within tissue n and moves toward the same boundary. Thus, in this study, there are 4 interfaces to consider. As displayed in Fig. 2, the first one B_1 corresponds to m = lumen and n = region comprising the intima, and is initialized inside the lumen. The second interface B_2 is initialized inside the intima-media and corresponds to m = region comprising the intima and n = lumen. The two interfaces meet at the boundary between the lumen and the intima. Similarly, the third interface B_3 corresponds to m = region comprising the media and n = surrounding, and is initialized inside the lumen and intima-media region. Finally, the fourth interface B_4 is located initially inside surrounding tissues and corresponds to m = surrounding and n = region comprising the media. These two interfaces meet at the EEM-adventitia boundary.

For that purpose, a speed function F is associated to each of the two interfaces, which should range between 0 and 1. The goal of the FMM is to construct the "arrival time" function $T(i, j)$ that satisfies the differential equation $|\nabla T|F = 1$. As in the case of [25], there is one arrival time function per interface, i.e., per speed function. When the algorithm stops, the two interfaces have met at the boundary and the speed functions are minimal. In this study, the speed function was based on two components: (1) a textural gradient inspired by [26]; and (2) the gray level gradient as in [19]. Thus, the former speed function is based on region information, whereas the latter is based on contour information. Although the former speed function is based on the B-mode PDF, it differs from the one adopted in [19].

The region-based speed function uses posterior probabilities in order to define a textural gradient. The purpose of the textural gradient is to locate the border between two regions presenting a difference in their gray level distributions (corresponding to different mixtures of gamma distributions), rather than to measure the data likelihood within a region. Two neighboring tissues m and n are considered with interface B moving within m toward n. Let v be the neighborhood of pixels (i, j) up winding the interface of the FMM. So, v is inside the tissue m. Let w be the neighborhood of pixels (i, j) down winding the interface. Thus, w falls eventually outside the tissue m, or equivalently inside the neighboring tissue n. See Fig. 2 for an illustration. Then, the proposed region-based speed function is of the form

$$F_{m,n}(i,j) = \left(1 + \left\{\frac{1}{N_v}\sum_{s\in v} P(s\in m|A_s)\right\} \times \left\{\frac{1}{N_w}\sum_{s\in w} P(s\in n|A_s)\right\} / \mu\right)^{-1} \quad (1)$$

The term $\{(1/N_v)\sum_{s\in v} P(s \in m|A_s)\} \times \{(1/N_w)\sum_{s\in w} P(s \in n|A_s)\}$ plays the role of a textural gradient, which is now explained. Firstly, the likelihood that a pixel s of v is actually inside the region m is denoted $P(A_s|m)$, while the likelihood that it is inside the region n is denoted $P(A_s|n)$. Here, A_s is the gray level of pixel s. Adopting the prior probabilities of each region $P(m) = P(n) = 1/2$, then, one obtains from Bayes' theorem the posterior probability that s is inside m in the form $P(s \in m|A_s) = P(A_s|m)/(P(A_s|m) + P(A_s|n))$. Similarly, the posterior probability that a pixel s of the neighborhood w is inside the region n is equal to $P(s \in n|A_s) = P(A_s|n)/(P(A_s|m) + P(A_s|n))$. The constant μ was automatically calibrated on each IVUS image, as explained below. By construction, the proposed speed function should be minimal at the boundary of the two tissues m and n, when the interface B matches the boundary between the two considered tissues.

The contour-based speed function uses the gray level gradient in the form:

$$F_{grad}(i,j) = (1 + |\nabla G_\sigma * A_s|/\lambda)^{-1}, \quad (2)$$

where ∇ is the gradient operator, G_σ is the 9×9 pixels symmetric Gaussian filter of standard deviation $\sigma = 3.5$. The size of the filter and the σ value were chosen to smooth the speckle inside the vessel components while keeping their boundaries. In this equation, λ is a normalizing constant that was calibrated with the constant μ so that the expressions within the parentheses in the right-hand side of Eq. (1) (related to the texture gradient) and Eq. (2) (related to the gray-level gradient) had the same average value c, i.e., $c = E[1 + \{(1/N_v)\sum_{s\in v} P(s \in m|A_s)\} \times \{(1/N_w)\sum_{s\in w} P(s \in n|A_s)\}/\mu] = E[1 + |\nabla G_\sigma * A_s|/\lambda]$, where E means average. In the reported tests, that average value was set equal to $c = 10$. Thus, the two speed functions had an average value around $1/c = 1/10$, which means that for each image, parameters μ and λ were calculated according to this fraction and the average values of the gradients in Eqs. (1) and (2). The parameter $c = 10$ was set empirically to produce speed function values close to zero near the boundaries. See Section 2.5 for details about the regions on which these average values were computed.

Globally, the proposed speed function of the current study was selected as the average of the components given in Eqs. (1) and (2):

$$F(i,j) = \frac{1}{2}F_{m,n}(i,j) + \frac{1}{2}F_{grad}(i,j). \quad (3)$$

Since the adopted values of the constants μ and λ were estimated, they allowed to calibrate the contribution of each type of gradient in the combined speed function.

2.3. Choice of the probability density function (PDF)

In [19], the Rayleigh PDF was chosen as the model for the gray level amplitude distribution of the ultrasonic speckle pattern in an IVUS B-mode image under the hypothesis of a uniform scattering tissue [22]. The Nakagami PDF is a more general model for the gray level amplitude distribution of the ultrasonic speckle pattern in a B-mode image as it takes into account the various possible configurations of ultrasound scatterers in a tissue [27]. The Nakagami distribution can be viewed as an approximation of the homodyned K-distribution [20] that is a statistical model for the echo envelope [21] and that is more easily handled. The Rayleigh distribution is a special case of the Nakagami distribution. Note that when the transducer center frequency is higher, the resolution cell is smaller, resulting in a lower scatterer's density, so that the distribution of the gray level in the B-mode image might depart from the Rayleigh distribution [27].

However, when a log-compression operator or various filters are applied to the B-mode image to improve visual perception, the Nakagami distribution might no longer be appropriate [28]. In such circumstances, the gamma PDF on the gray level amplitude was tested, in [29], as a valid approximation in the case of B-mode images in the context of clinical cardiac images. See also [30] for a similar study. Recall that the gamma distribution on the amplitude A_s is defined by:

$$\mathcal{G}(A_s|k,\theta) = \frac{A_s^{k-1}}{\Gamma(k)\theta^k} e^{-A_s/\theta}, \quad (4)$$

where $k > 0$ is a shape parameter, Γ is the Euler gamma function, and $\theta > 0$ is a scaling parameter. The mean and variance of this PDF are equal to $k\theta$ and $k\theta^2$, respectively.

A model of mixtures of gamma distributions for the gray level of B-mode images was adopted for the post-processed B-mode

Author's personal copy

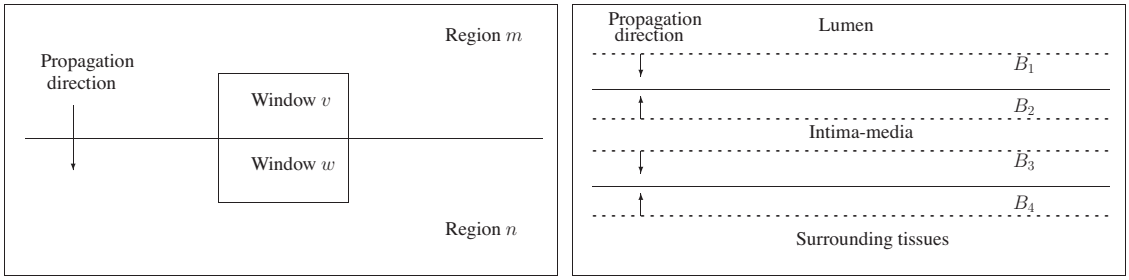

Fig. 2. Left: illustration of the nomenclature used in Eq. (1). Right: illustration of the 4 interfaces used in our implementation of the FMM algorithm; full lines represent the searched boundaries, whereas dashed lines are moving boundaries of the FMM algorithm, where B_1–B_2 are moving in opposite directions to define the lumen-intima boundary and B_3–B_4 are also moving in opposite directions to define the EEM boundary.

images of our study. This strategy provided enough flexibility for modeling the echogenicity of the lumen (blood), vessel wall (plaque) and tissues surrounding the coronary artery. So, in the definition of the region-based function of Eq. (1), mixtures of gamma distributions were used as likelihoods in order to compute the posterior probabilities $P(s \in m|A_s)$ and $P(s \in n|A_s)$. The parameters of the gamma mixture distributions were estimated with the Expectation-Maximization (EM) algorithm [31], as adapted to mixtures of gamma distributions in [32, Table I]. The EM algorithm was initialized with a clustering based on the four quantiles of the gray level intensities. The initial parameters for the first gamma PDF were thus computed on the lowest 25% of the data; the initial parameters for the following PDFs of the mixture were respectively computed with the following quartiles of the data.

The number of gamma distributions ℓ was set empirically to 4. The 4 estimated gamma distributions were classified by increasing order of means. Then, the distributions were combined as follows in order to represent the four relevant tissues or artifacts present within images:

$$P(A_s|j) = \sum_{i=1}^{4} p_{i,j}\mathcal{G}(A_s|k_i, \theta_i), \tag{5}$$

where the index $j = 1, 2, 3, 4$ represents the guide wire and the lumen, a region comprising the intima (inside the intima-media), a region comprising the media (inside the EEM) and the surrounding tissues (outside the EEM), respectively, as well as any other artifact present within the tissue (calcium, its shadow cone, stent, side branches). In Eq. (5), A_s represents the gray level of pixel s, $\mathcal{G}$ is the gamma distribution of Eq. (4) and the index $i = 1, 2, 3, 4$ represents each gamma distribution of the mixture. The proportions $p_{1,j}, \ldots, p_{4,j}$ of each gamma distribution in the mixture representing the tissue j are non-negative real numbers that satisfy $\sum_{i=1}^{4} p_{i,j} = 1$. These proportions for each tissue j were estimated based on the initial interpolated lumen and EEM boundaries discussed in Section 2.4.

In the case of the IVUS images of the database of this study, some of them presented a large number of pixels with gray level varying between 0 and 3 (on the scale of [0, 255]). It was observed that the presence of a peak in the histogram of gray levels caused the EM algorithm to get stuck with only two classes of hidden labels, even when the number of such classes was set to ℓ=4, due to an exceedingly small variance of the gamma distribution corresponding to the peak. The solution consisted in imposing a lower bound on the variance of the distribution.

2.4. Manual initialization of the FMM segmentation algorithm

The FMM requires initial contours representing approximate boundaries between the lumen and the intima, and between the media and the adventitia, respectively. The initial radial contours of all frames were determined from manually traced boundaries on two longitudinal cuts (L-views) of the IVUS sequence corresponding to two planes at equally spaced angles. In brief, the operator selected, for each L-view and for each vessel region to segment (lumen-intima or media-adventitia boundary), two longitudinal lines (one on each side of the catheter) of 10.7 ± 2.3 control points that were interpolated to produce boundary points for each 2D cross-sectional image of the whole 3D sequence. By considering the 2 L-views, this yielded four contour points in each 2D frame that were spline-interpolated radially to obtain each closed approximate initial boundary (lumen-intima and media-adventitia) that were forbidden to overlap (see Fig. 3). The images (in the polar domain) corresponding to a given position in the pullback were also available while doing the manual initialization for additional visualization (but not for entering control points).

2.5. Implementation of the FMM algorithm

The following description explains the implementation of the FMM algorithm on each image of an IVUS sequence for defining the media-adventitia boundary, and then the lumen-intima interface.

For the media-adventitia boundary, we started with the initial interpolated contour obtained by the manual initialization (Section 2.4). The initial interface B_4 for the FMM was obtained by translating radially the initial contour 0.4 mm in the direction of surrounding tissues (i.e., outward). The desired boundary should thus be within a 0.4 mm distance from the initial contour (see Fig. 3, left image). Another interface B_3 was obtained by translating radially the same contour 0.4 mm toward the center of the artery (i.e., inward). Note that the proportions $p_{i,j}$ for $i = 1, 2, 3, 4$ in Eq. (5), for the surrounding tissues ($j = 4$) and the region comprising the media ($j = 3$) between B_3 and the EEM, were computed with the EM algorithm of [33], based on the initial interpolated EEM contour and the two initial interfaces B_3 and B_4. Also, the parameters μ and λ in Eqs. (1) and (2), respectively, were estimated for the interface B_4 on the region within the initial positions of the interfaces B_3 and B_4; those constants were estimated similarly for the interface B_3. When the FMM stops, the two interfaces B_3 and B_4 have met at the boundary between the EEM of the media and surrounding tissues (see Fig. 2). Note that if the intima-media is thinner than 0.4 mm, the region between B_3 and the EEM will comprise other tissues than the media. Note also that B_3 will eventually be located inside the media during the propagation of the interfaces.

Next, an initial contour representing the boundary between the lumen and the intima was considered. The initial interface B_2 for the FMM was also obtained by translating it 0.4 mm outward, but no further than the EEM boundary. Another interface B_1 was obtained by translating the same initial contour 0.4 mm inward, but no further than the IVUS catheter. Then, the FMM was applied as above, using the appropriate speed functions. Again, note that B_2 will eventually be located inside the intima during the propagation of the interfaces.

Author's personal copy

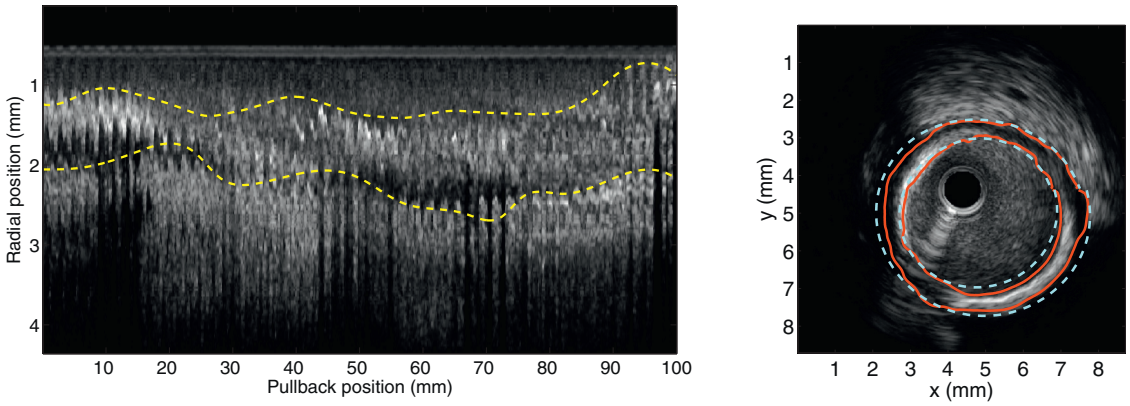

Fig. 3. Left: example of initial manually traced boundaries (yellow dashed curves) on half a longitudinal cut of a pullback. Right: example of a cross-section that presents a calcified area from that in vivo sequence pullback; the red full curves represent the lumen and EEM contours detected with the FMM algorithm; the light blue dashed curves represent the contours obtained by b-spline interpolating the manually traced boundaries on the L-views. (For interpretation of the references to color in this figure legend, the reader is referred to the web version of the article.)

For convenience, all ungated IVUS images were expressed into polar coordinates (with 512 values for the angle and half the size of the Cartesian image for the radius). The FMM was applied to the resulting 2D images. We chose not to apply the FMM on the 3D volume due to the cardiac motion discontinuities in the sequences caused by the lack of ecg-gating. Also, the IVUS catheter displayed as a black circle on the images was removed automatically before using the FMM. Finally, a simple Gaussian smoothing filter was applied to the segmented boundaries, after the segmentation process. Namely, the contour was smoothed by applying radially the Gaussian filter [0.1, 0.2, 0.4, 0.2, 0.1], and once again with the filter [0.1, 0, 0.2, 0, 0.4, 0, 0.2, 0, 0.1]. This operator amounts to setting a prior on the smoothness of the contours.

2.6. Reproducibility of the FMM with regard to random perturbations

To test the robustness of the FMM with regard to the manual initialization, we performed the following reproducibility study. For each L-view, every interpolated point on each 2D frame that was moved radially by ±0.4 mm to define the initial boundaries B_1–B_4 (Fig. 2), was perturbed randomly in the radial direction by ±0.05, ±0.1, ±0.2 and ±0.3 mm (according to a uniform distribution). The range of these perturbations included the measured average distance between manually drawn contours by different users of 0.06–0.18 mm [18,19]. Then, the eight randomly perturbed contour points of each searched boundary were spline-interpolated radially, as mentioned earlier, to form a closed contour. The performance of the FMM segmentation was then tested again with those new initial contours.

2.7. Data analysis

Once having all manual segmentations for quantitative comparisons, the analysis steps involved the manual initialization on L-views, the computation of the performance metrics, the comparison of results between datasets 1 and 2, the reproducibility analysis that aimed to determine the robustness to the manual L-view initializations, and comparison of vessel wall areas (plaque areas for IVUS images with atherosclerosis) between manual and computed segmentations. Note that the manual gold standard segmentations and manual initializations were performed independently by different technicians. The time required for the manual L-view initializations was on average 3 min and 46 s per sequence. This included viewing the IVUS video, displaying the 4 half L-views, and clicking of control points on each estimated boundary.

The algorithmic FMM segmentation was applied to all frames of each sequence, for a total of 82,848 images. Thus, contours were detected even on the frames that did not have to (78,706 frames) or could not be (935 frames) manually segmented by the technicians. The time required to segment both boundaries (lumen-intima and EEM-adventitia) of each sequence was on average 7 min and 23 s. This corresponds approximately to a processing time of 0.42 s per 2D IVUS image. Optimization of the Matlab code and parallelization would improve processing time.

2.7.1. Performance metrics of the FMM segmentations

For each of the 3207 frames where both lumen-intima and EEM-adventitia contours were segmented by the technicians, we compared the manual segmentation with the segmentation obtained by the proposed method.

We considered the mean point-to-point and Hausdorff distances [34] between the algorithmic and manual segmentations in mm. We also computed these distances relative to the largest diameter of the contour obtained by the manual segmentation (i.e., the largest distance between two points of that contour). Namely, if *MD* represents the mean point-to-point distance between contours at a given frame, and if *D* is the diameter of the manual contour at that frame, then we considered the ratio $MD/D \times 100\%$. We then computed the average of the mean distance *MD* as well as the ratio $MD/D \times 100\%$ over all manually segmented frames of each sequence. We similarly computed the average of *HD* and of $HD/D \times 100\%$ for the Hausdorff distance *HD* over all manually segmented frames of each sequence.

We also used the error of area [2,4,7,35,36] as another performance assessment metric. Namely, if *A* represents the area obtained by the algorithmic segmentation and *B* is the area of the manual segmentation, then the error of area *EA* is defined by $|A - B|$ in mm^2 (note the absolute value). We also computed the relative error of area $|A - B|/B \times 100\%$. These values for the lumen and EEM areas were averaged over all manually segmented frames of each sequence. Some studies [6,37–39] defined the error of area as $(A - B)/B \times 100\%$, which of course decreases significantly the value of the measure. Indeed, when averaged over all frames, positive and negative biases may cancel. This last measure may underestimate the true error of area unless *A* is always considered as the largest surface.

As additional assessment metrics, the plaque areas and plaque areas normalized by the EEM surfaces were computed for all datasets 1 and 2 sequences. For each frame for which both the lumen and the EEM could be manually segmented by the technicians, we considered the ratio $|P - Q|/Q \times 100\%$, where *P* is the

Author's personal copy

Table 2
Comparison of the mean point-to-point (MD) and Hausdorff (HD) distances, and of the errors of areas (EA) for the lumen-intima and EEM-adventitia boundaries for IVUS images from datasets 1 and 2.

		Dataset 1 ($n = 35$ sequences with 1388 frames)	Dataset 2 ($n = 43$ sequences with 1819 frames)	p-Value
MD (mm)	Lumen	0.10 ± 0.03	0.13 ± 0.03	<0.001
		$(3.3 \pm 0.7\%)$	$(4.5 \pm 1.5\%)$	<0.001
	EEM	0.10 ± 0.03	0.10 ± 0.03	0.252
		$(2.4 \pm 0.6\%)$	$(2.4 \pm 0.7\%)$	0.880
HD (mm)	Lumen	0.31 ± 0.07	0.34 ± 0.08	0.064
		$(10.2 \pm 1.8\%)$	$(12.0 \pm 2.3\%)$	<0.001
	EEM	0.32 ± 0.09	0.30 ± 0.09	0.388
		$(7.6 \pm 2.0\%)$	$(7.6 \pm 2.0\%)$	0.778
EA (mm^2)	Lumen	0.43 ± 0.17	0.53 ± 0.19	0.009
		$(6.9 \pm 2.6\%)$	$(11.1 \pm 7.2\%)$	0.002
	EEM	0.58 ± 0.31	0.52 ± 0.25	0.422
		$(4.3 \pm 1.8\%)$	$(4.6 \pm 2.3\%)$	0.960

plaque area computed with the FMM, whereas Q is the manually segmented plaque area. Those ratios were averaged over all manually segmented frames of each sequence.

We also computed, on each frame, the error of plaque area relatively to the EEM surface. The ratio $|P - Q|/R \times 100\%$ was considered, where P remains the plaque area computed with the algorithmic segmentation, Q is still the plaque area computed manually, and R is the EEM area computed from the manual segmentation. This error ratio was also averaged over all manually segmented frames of each sequence.

3. Results

3.1. Performance metrics of the FMM segmentations

On average over all sequences, the mean point-to-point and Hausdorff distances for the lumen contours were 0.11 ± 0.03 mm ($4.0 \pm 1.4\%$) and 0.33 ± 0.07 mm ($11.2 \pm 2.3\%$), respectively. Recall that there are 3207 frames in all performance assessments and that values in parenthesis are $MD \times 100/D$ and $HD \times 100/D$, respectively. The mean point-to-point and Hausdorff distances for the EEM contours were 0.10 ± 0.03 mm ($2.4 \pm 0.7\%$) and 0.31 ± 0.09 mm ($7.6 \pm 2.0\%$), respectively. On average, errors of areas were $0.49 \pm 0.18\ mm^2$ ($9.3 \pm 6.0\%$) for the lumen and $0.55 \pm 0.28\ mm^2$ ($4.5 \pm 2.1\%$) for the vessel external boundary, when averaged over all sequences. Numbers in parenthesis are relative errors of areas.

We compared the performance of the FMM versus manual "gold standard" segmentations for both types of IVUS sequences. As can be seen in Table 2, there were no significant differences for the EEM interface between the datasets 1 and 2 sequences (unpaired t-tests, $p > 0.05$). On the other hand, all performance metrics between the manual and the automatic segmentations of the lumen interface were significantly better for dataset 1 (unpaired t-tests, $p < 0.05$), except for the Hausdorff distance.

3.2. Reproducibility of the FMM segmentations for dataset 1

The reproducibility of the L-view manual initializations to random perturbations was limited to dataset 1 since the Hausdorff distances (in mm) turned out to be equivalent between datasets 1 and 2 (see Table 2). Moreover, there was no significant differences in the various performance metrics for the EEM. The results of this analysis are summarized in Table 3. To compare each measure corresponding to different random initializations, we performed multiple comparisons with respect to the case where no random perturbation was applied using an analysis of variance (Kruskal–Wallis one-way analysis of variance on ranks with Tukey test for multiple comparisons whenever normality test failed, or else, Holm–Sidak method). Note that for this analysis, a perturbation of the initialization by 1 mm corresponds to about 70.9% of the lumen radius and 50.6% of the EEM radius. Therefore, the reproducibility analysis considers perturbations of the initialization within $\pm 3.5\%$ to $\pm 21.3\%$ of the lumen radius, and $\pm 2.5\%$ to $\pm 15.2\%$ of the EEM radius.

As shown in Table 3, a perturbation of ± 0.1 mm (in the radial direction) did not affect the performance metrics for the lumen as well as for the EEM. This finding reveals the stability of the FMM segmentation for such a perturbation. For random displacements of the initialization by ± 0.2 mm, only the Hausdorff EEM distances and the EEM errors of area in mm^2 were not affected ($p > 0.05$). All performance metrics were significantly increased following perturbations of ± 0.3 mm ($p < 0.05$). The performances of the FMM algorithm are thus degraded by such perturbations of the initialization. Nevertheless, the mean point-to-point distances, Hausdorff distances as well as errors of area remained acceptable (all performance metrics were, on average, below 13.1%).

3.3. Plaque areas

On average, the errors of plaque area between manually and automated segmentations were $14.6 \pm 12.3\%$ for all sequences (for a total of 3207 frames). This error was equivalent for dataset 1 ($14.0 \pm 8.3\%$) and dataset 2 ($15.1 \pm 14.9\%$, $p > 0.05$). The errors of plaque area normalized by the EEM surfaces for all sequences were $5.4 \pm 2.2\%$. This error was equivalent for dataset 1 ($5.5 \pm 1.7\%$) and dataset 2 ($5.4 \pm 2.6\%$).

3.4. Frames that presented artifacts

Out of the 1388 dataset 1 images that were manually segmented by the technicians, there were 209 of them that presented a difficulty in the manual segmentation due to one or more artifacts (see Table 1). To compare the Hausdorff and mean point-to-point distances between the segmented contours and the validation contours for the lumen and the EEM, as well as the difference of areas corresponding to each category, we performed multiple comparisons with respect to the case where no comment was written using an analysis of variance (Kruskal–Wallis one-way analysis of variance on ranks with Dunn's method for multiple comparisons). The comparisons are presented in Table 4. As shown, none of the artifacts in the images (c.f. Table 1) affected the performance metrics for the lumen or for the EEM, when compared with category 1 (i.e., no comment on artifacts). This finding suggests the stability of the FMM segmentation under such artifacts. Note, however, that some of the categories had few samples. So, the algorithm would

Author's personal copy

Table 3
Comparison of the mean point-to-point (MD) and Hausdorff (HD) distances, and of the errors of areas (EA) for the lumen-intima and EEM-adventitia boundaries ($n = 35$ sequences from the 1388 frames of dataset 1) using random perturbations of the four longitudinal views that were used for the initialization. The random perturbations were within ±0.05, ±0.1, ±0.2 and ±0.3 mm (in the radial direction). The reference group corresponds to no random perturbation (i.e., 0 mm, thus being the initial manual initialization).

		Reference 0 mm	Perturbation ±0.05 mm	Perturbation ±0.1 mm	Perturbation ±0.2 mm	Perturbation ±0.3 mm
MD (mm)	Lumen	0.10 ± 0.03 (3.3 ± 0.7%)	0.10 ± 0.02 (3.3 ± 0.7%)	0.10 ± 0.02 (3.4 ± 0.7%)	0.11 ± 0.02* (3.8 ± 0.7%)*	0.14 ± 0.03* (4.5 ± 0.8%)*
	EEM	0.10 ± 0.03 (2.4 ± 0.6%)	0.10 ± 0.03 (2.4 ± 0.6%)	0.11 ± 0.03 (2.5 ± 0.6%)	0.12 ± 0.03* (2.9 ± 0.6%)*	0.15 ± 0.03* (3.5 ± 0.6%)*
HD (mm)	Lumen	0.31 ± 0.07 (10.2 ± 1.8%)	0.32 ± 0.07 (10.3 ± 1.8%)	0.32 ± 0.07 (10.6 ± 1.7%)	0.35 ± 0.07 (11.4 ± 1.7%)*	0.40 ± 0.08* (13.1 ± 2.1%)*
	EEM	0.32 ± 0.09 (7.6 ± 2.0%)	0.32 ± 0.09 (7.7 ± 2.0%)	0.33 ± 0.09 (7.8 ± 2.0%)	0.36 ± 0.08 (8.6 ± 1.9%)	0.41 ± 0.08* (9.8 ± 1.9%)*
EA (mm^2)	Lumen	0.43 ± 0.17 (6.9 ± 2.6%)	0.44 ± 0.17 (7.1 ± 2.7%)	0.47 ± 0.16 (7.4 ± 2.5%)	0.56 ± 0.22* (8.8 ± 2.8%)*	0.71 ± 0.21* (11.1 ± 2.7%)*
	EEM	0.58 ± 0.31 (4.3 ± 1.8%)	0.60 ± 0.31 (4.4 ± 1.8%)	0.63 ± 0.30 (4.7 ± 1.7%)	0.76 ± 0.34 (5.7 ± 1.8%)*	0.92 ± 0.35* (7.1 ± 1.6%)*

* $p < 0.05$.

Table 4
Comparison of the mean point-to-point (MD) and Hausdorff (HD) distances, and of the errors of areas (EA) for the lumen-intima and EEM-adventitia boundaries (dataset 1 with 1388 images) within the eight categories of comments written by the technicians (Table 1). The reference group (category 1) corresponds to no comment.

	MD (mm)		HD (mm)		EA (mm^2)	
	Lumen	EEM	Lumen	EEM	Lumen	EEM
Cat. 1 ($n = 1179$)	0.097 ± 0.045	0.102 ± 0.047	0.304 ± 0.137	0.326 ± 0.153	0.424 ± 0.393	0.590 ± 0.550
Cat. 2 ($n = 20$)	0.105 ± 0.039	0.087 ± 0.026	0.338 ± 0.122	0.267 ± 0.083	0.257 ± 0.186	0.432 ± 0.350
Cat. 3 ($n = 91$)	0.091 ± 0.034	0.120 ± 0.048	0.299 ± 0.115	0.366 ± 0.135	0.366 ± 0.303	0.580 ± 0.459
Cat. 4 ($n = 72$)	0.079 ± 0.025	0.104 ± 0.039	0.286 ± 0.105	0.304 ± 0.098	0.480 ± 0.291	0.976 ± 0.659
Cat. 5 ($n = 8$)	0.131 ± 0.060	0.079 ± 0.017	0.374 ± 0.163	0.198 ± 0.047	0.221 ± 0.194	0.434 ± 0.407
Cat. 6 ($n = 10$)	0.105 ± 0.049	0.089 ± 0.032	0.330 ± 0.116	0.282 ± 0.081	0.346 ± 0.299	0.546 ± 0.347
Cat. 7 ($n = 4$)	0.275 ± 0.058	0.171 ± 0.100	0.728 ± 0.123	0.491 ± 0.264	0.907 ± 0.894	0.993 ± 1.214
Cat. 8 ($n = 4$)	0.078 ± 0.009	0.131 ± 0.036	0.260 ± 0.052	0.536 ± 0.155	0.226 ± 0.134	0.697 ± 0.384

have to be tested on a large number of images with such artifacts and compared with manual segmentations in order to confirm its robustness. The multiple comparisons also showed the following findings: (1) the mean point-to-point distance for the lumen with a stent (category 4) is significantly better than in the presence of branching and calcium (category 7); (2) the Hausdorff distance for the EEM is significantly better in the presence of calcium and dissection (category 5) than with a contrasting agent (category 8); (3) the error of area for the EEM is significantly better in the presence of dissection (category 2) than with a stent (category 4). Aside from these exceptions, there were no significant differences between the various categories for all metrics.

Table 5
Summary of the errors of area (EA) and of the mean point-to-point (MD) and Hausdorff (HD) distances for the lumen and the EEM according to the literature before 2006. The parameter n is the number of IVUS images used for the validation. The type of algorithm is indicated: fully automatic (F), semi-automatic (S) and/or interactive (I) (possibly only for the initialization – init.).

	Type	Lumen				EEM			
		EA (mm^2 or %)	MD (mm or %)	HD (mm)	n	EA (mm^2 or %)	MD (mm or %)	HD (mm)	n
Sonka et al. 1995 [41][a]	I (init.)	1.13 mm^2	0.07 ± 0.02 mm		38	1.33	0.09 ± 0.03 mm		38
Li 1997 [37]	S-I	−0.21 ± 0.342 mm^2[b]			127	0.27 ± 0.492 mm^2[b]			127
	S-I	−0.80 ± 7.283%[c]			4000	0.17 ± 4.443%[c]			4000
Mojsilovic et al. 1997 [42]	F	0.19 ± 0.18 mm^2			29	0.68 ± 0.39 mm^2			29
Zhang et al. 1998 [43]	I		0.13 ± 0.05 mm		30		0.17 ± 0.08 mm		30
Haas et al. 2000 [44]	F		−1.9 ± 10.5%		29		−2.9 ± 7.6%		29
Klingensmith et al. 2000 [45]	S	0.60 (WI)[d]	0.65 (WI)[d]		185	0.81 (WI)[d]	0.68 (WI)[d]		185
Kovalski et al. 2000 [35]	F	15.2 ± 17.4%			44	6.5 ± 7.6%			44
Takagi et al. 2000 [38]	F	−0.15 ± 0.84 mm^2			193	−0.18 ± 1.36 mm^2			78[e]
		0.4 ± 14.4%			193	0.6 ± 9.7%			78[e]
Bovenkamp 2004 [39]	F	−0.14 ± 1.01 mm^2			1067	0.13 ± 2.16 mm^2			1067
Brusseau et al. 2004 [2]	F	0.70 ± 0.48 mm^2	0.10 ± 0.03 mm		15				
		8.2 ± 5.4%			15				
Plissiti et al. 2004 [46]	I (init.)	4.9%[f]			18	2.1%[f]			18
Present study	S	0.49 ± 0.18 mm^2	0.11 ± 0.03 mm	0.33 ± 0.07 mm	3207	0.55 ± 0.28 mm^2	0.10 ± 0.03 mm	0.31 ± 0.09 mm	3207
		9.3 ± 6.0%	4.0 ± 1.4%	11.2 ± 2.3%	3207	4.5 ± 2.1%	2.4 ± 0.7%	7.6 ± 2.0%	3207

[a] The validation was performed with in vitro IVUS images.
[b] Validation from the study by [47].
[c] Validation from the study by [40], variability between different segmentation users was calculated and the results have not been compared with manually traced contours.
[d] The Williams index (WI) is the ratio of the average observer-observer variability to the average computer-observer variability [45].
[e] Images used for the validation of a total of 270.
[f] Percentage of volume error for whole sequences.

Author's personal copy

Table 6
Summary of the errors of area (EA) and of the mean point-to-point (MD) and Hausdorff (HD) distances for the lumen and the EEM according to the literature of the past 7 years. The parameter n is the number of IVUS images used for the validation. The type of algorithm is indicated: fully automatic (F), semi-automatic (S) and/or interactive (I) (possibly only for the initialization – init.).

	Type	Lumen				EEM			
		EA (mm^2 or %)	MD (mm or %)	HD (mm)	n	EA (mm^2 or %)	MD (mm or %)	HD (mm)	n
Gil et al. 2006 [48]	F					$8.60 \pm 3.34\%$	0.23 ± 0.07 mm		540
Whale et al. 2006 [3]	F		0.180 ± 0.027 mm		3288		0.200 ± 0.069 mm		3288
Giannoglou et al. 2007 [49]	F	0.70 ± 1.34 mm^2			50	0.17 ± 2.29 mm^2			50
Sanz-Requena et al. 2007 [4]	S	11.095%[a]			408	4.985%[a]			408
	I	10.956%[b]			408	7.276%[b]			408
Taki et al. 2008 [9]	F	6.27 ± 1.73 mm^2	0.20 ± 0.15mm	0.71 ± 0.25 mm	60	5.02 ± 3.79 mm^2	0.21 ± 0.05 mm	0.45 ± 0.31 mm	60
Unal et al. 2008 [5]	F	0.60 ± 0.99 mm^2	0.08 ± 0.10 mm	0.44 ± 0.76 mm	1272	0.49 ± 0.76 mm^2	0.07 ± 0.08 mm	0.84 ± 1.74 mm	1272
				0.65 ± 1.27 mm[c]	647			0.98 ± 1.78 mm[c]	647
Papadogiorgaki et al. 2008 [12]	F	0.17 ± 1.34 mm^2[d]			320	0.03 ± 1.53 mm^2[d]			320
Downe et al. 2008 [10]	I	2.709 mm^2	0.117 mm[a]		15[e]	2.726 mm^2	0.097 mm[a]		15[e]
Ciompi et al. 2009 [6]	F	0.08 ± 0.24 mm^2			10				
Bovenkamp et al. 2009 [11]	S-I	0.20 ± 0.69 mm^2[a]			1067	-0.37 ± 0.55 mm^2[a]			1067
Katouzian et al. 2010 [13]	F	86–88% (TP)			205				
Moraes et al. 2011 [14]	F	$10.7 \pm 11.7\%$ (FP)			1300	$9.1 \pm 17\%$ (FP)			1300
		$7.3 \pm 7.5\%$ (FN)				$8.1 \pm 6.7\%$ (FN)			
Ciompi et al. 2012 [16]	F					0.594 mm^2, 10.1%	0.211 mm	0.528 mm	522
Mendizabal-Ruiz et al. 2013 [15]	F			13.4 ± 3.8% (Obs. 1)	585				
				14.6 ± 5.3% (Obs. 2)					
Present study	S	0.49 ± 0.18 mm^2	0.11 ± 0.03 mm	0.33 ± 0.07 mm	3207	0.55 ± 0.28 mm^2	0.10 ± 0.03 mm	0.31 ± 0.09 mm	3207
		$9.3 \pm 6.0\%$	$4.0 \pm 1.4\%$	$11.2 \pm 2.3\%$	3207	$4.5 \pm 2.1\%$	$2.4 \pm 0.7\%$	$7.6 \pm 2.0\%$	3207

[a] Interactive version of the segmentation.
[b] Version with initialization of the segmentation.
[c] Segmentation with feature detection for the more challenging second test dataset.
[d] Texture and low-pass filtering version of the algorithm.
[e] Number of patients.

3.5. Examples of segmentations

A few examples of segmentations are presented in Figs. 4–6. In these 2D examples taken from each sequence considered, full line contours correspond to the algorithmic FMM segmentations, whereas dashed lines represent the "gold standard" manual segmentations of the lumen-intima and EEM-adventitia boundaries. Results from dataset 1 are presented in Fig. 4 followed by examples of dataset 2 results in Fig. 5. In Fig. 6, typical segmentations from dataset 1 are presented for different categories of artifacts noted by the expert technicians while doing the manual segmentation (c.f. Table 1).

4. Discussion

As can be seen from Tables 5 and 6, our study is the most important of the literature with [3] as far as the number of images used for the comparison of algorithmic and manual segmentations is concerned ($n = 3207$).[3] Our validation came from sequences acquired on 35 patients, which allowed insuring a good statistical sampling since datasets 1 and 2 consisted of 3207 regularly spaced frames from an original database of 82,848 images. We believe that this reduced the chance of having too many similar frames in the validation datasets (since adjacent frames from an IVUS pull-back are likely to present similarities). Besides, it could be noticed that our results are based on manually segmented images that included problematic situations as the presence of a stent, calcium inclusions within the atherosclerotic plaque, lateral coronary branches, catheter frictions within the narrowed vessel lumen, injection of a contrast agent, and artery dissections. Note that the proportion of frames where the lumen-intima and EEM-adventitia interfaces could be detected by the IVUS core laboratory experts was similar for both "iLab" and "Galaxy II" databases. Indeed, 77.9% of the 1782 "iLab" images (one out of twenty images of all sequences, $n = 1388$) and 77.1% of the 2360 "Galaxy II" selected frames ($n = 1819$) could be segmented manually to constitute datasets 1 and 2, respectively.

As mentioned in [50], direct comparisons between algorithms can only be made from tests performed on a common database. For that purpose, let us mention [51], written by the organizers of the IVUS Segmentation Challenge that was part of the 2011 Medical Image Computing and Computer Assisted Intervention (MICCAI) workshop on Computing and Visualization for (Intra) Vascular Imaging (CVII). In that paper, the proposed segmentation method was compared with other methods in the context of the IVUS Segmentation Challenge, based on a common database. Nevertheless, we present an indirect comparison of IVUS segmentation algorithms based on reported results. Note that in [51, Figs. 8 and 9], examples of segmentation results obtained from the methods of the various participants versus the ground truth annotations are given, some of them including artifacts.

One can also see from Tables 5 and 6 that errors of area reported in the literature were within 0.19 and 1.13 mm^2 [2,5,41,42,49] (or 8.2% and 15.2% [2,4,14,35]) for the lumen, and within 0.17–1.33 mm^2 [5,16,41,42,49] (or 5.0% and 9.1% [4,14,35,48]) for the EEM. On average, we have obtained an error of area of 0.49 mm^2 (or 9.3%) for the lumen and of 0.55 mm^2 (or 4.5%) for the EEM. Of these methods, [2,5,14,35,42,48,49] are fully automatic. Here, we did not include the studies [6,11,12,37–39], because the difference of area was not considered in absolute value, which decreased significantly its mean value, as noted in Section 2.7.1. We did not include the study [46] because volumetric measurements were provided. Note that the errors of area reported in [9,10] are much higher (i.e., above 2.7 mm^2). Our results are thus comparable to other studies, despite the fact that our validation was performed on more than 3000 images, without excluding any image for which

[3] The study [40] used by [37] was realized with 4000 images. However, the reported results correspond to the variability of the algorithm under different users. These results do not correspond to a comparison with manually traced contours by expert technicians.

Author's personal copy

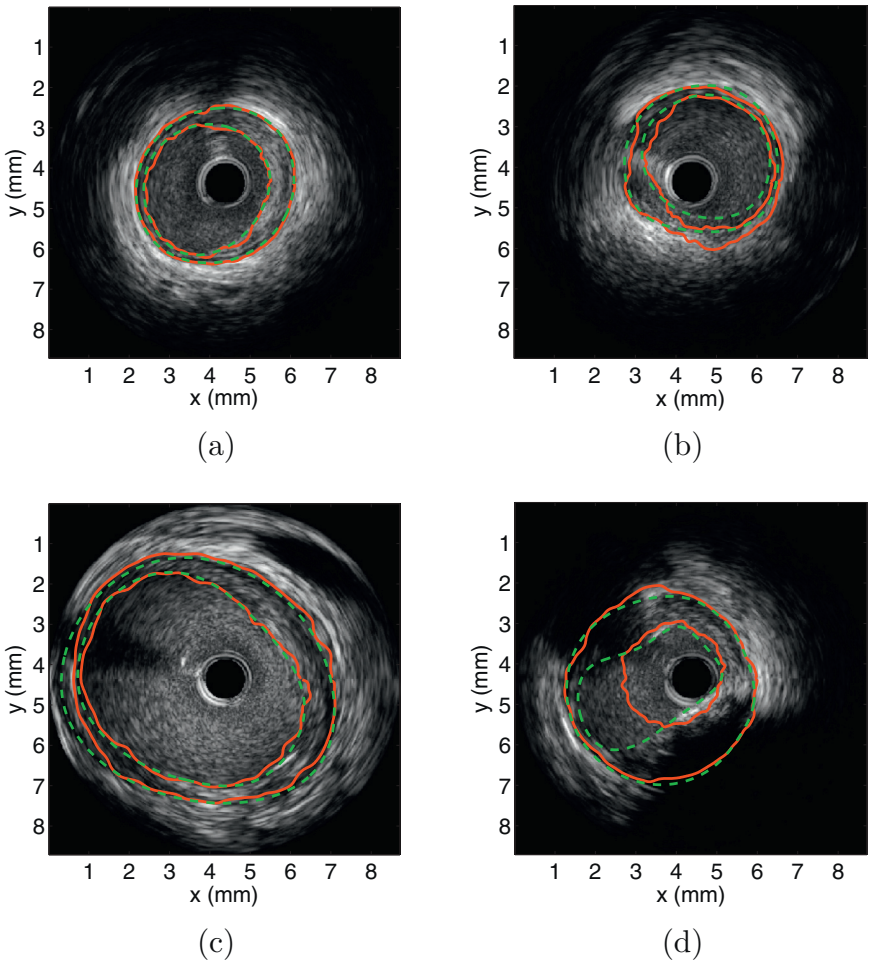

Fig. 4. First row: two frames from a dataset 1 sequence for which the combined Hausdorff distances (HD) for the lumen and EEM boundaries were the lowest (good concordance between algorithmic and manual segmentations). When averaged over the whole sequence, the HD for the lumen was 0.242 ± 0.068 mm, whereas it was 0.179 ± 0.061 mm for the EEM. Second row: two frames of another dataset 1 sequence for which combined HD for the lumen and EEM boundaries were highest (poor concordance between algorithmic and manual segmentations). When averaged over the whole sequence, the HD for the lumen was 0.588 ± 0.272 mm, whereas it was 0.393 ± 0.166 mm for the EEM. FMM segmentations (red full lines) compared with manual segmentations (green dashed lines). Frames with the best segmentation of each sequence (a) and (c). Frames with the worse segmentation of each sequence (b) and (d). (For interpretation of the references to color in this figure legend, the reader is referred to the web version of the article.)

the lumen and the EEM could be both manually segmented with certainty (even if artifacts were present). As also noted in these tables, our results are comparable to the study of [4] that was validated with only 408 IVUS images.

As reported in Section 3.1, the mean point-to-point and Hausdorff distances were on average 0.10 and 0.31 mm (or 2.4% and 7.6%), in the case of the EEM. This is a very interesting result since the EEM can be especially difficult to segment in the case of images with stents, calcium nodules and coronary bifurcations. Note that from Tables 5 and 6, the mean distance for the EEM varies between 0.07 and 0.23 mm [3,5,9,10,16,41,43,48] and the Hausdorff distance between 0.45 and 0.98 mm [5,9,16]. Of these studies, [3,5,9,16,48] presented fully automatic segmentation methods. We excluded [44] from that comparison since signed distances were considered in that study, which decreases significantly the measure. Another important challenge of our study was to validate the robustness of the FMM segmentation in the case of IVUS images acquired with a 40 MHz catheter. Indeed, our previous study [19] was performed on femoral arteries using 20 MHz IVUS catheters; that lower frequency reduces considerably artifacts caused by blood speckle into the lumen, which helps the segmentation task. Our mean point-to-point and Hausdorff distances were 0.11 and 0.33 mm (or 4.0% and 11.2%) for the lumen, which is very acceptable. As indicated in Table 5, only the study [44] reported mean point-to-point distances in percents.[11] However, this study included only 29 IVUS images, which is not representative of the clinical reality.

To assess whether the proposed segmentation method was significantly better than the method of [19] (that was developed for femoral artery IVUS segmentation) in the context of IVUS coronary imaging, the segmentations of the EEM and lumen boundaries were performed on datasets 1 and 2 using the region-based speed function of [19] with the same initialized boundaries. All measures were significantly better with the proposed implementation (that is based on gamma distributions, the textural gradient, and with weights between the region-based and gradient speed functions automatically adjusted) than with the implementation based on [19] (that is based on Rayleigh distributions, the PDF-region-based speed function, and with fixed weights between the region-based and gradient speed functions automatically adjusted); the p-values

[11] Studies usually do not report Hausdorff distances, as far as we can tell; that severe performance metric is not always advantageous to be shown. Acceptable results were obtained in the present study, better than the ones reported in [5].

Author's personal copy

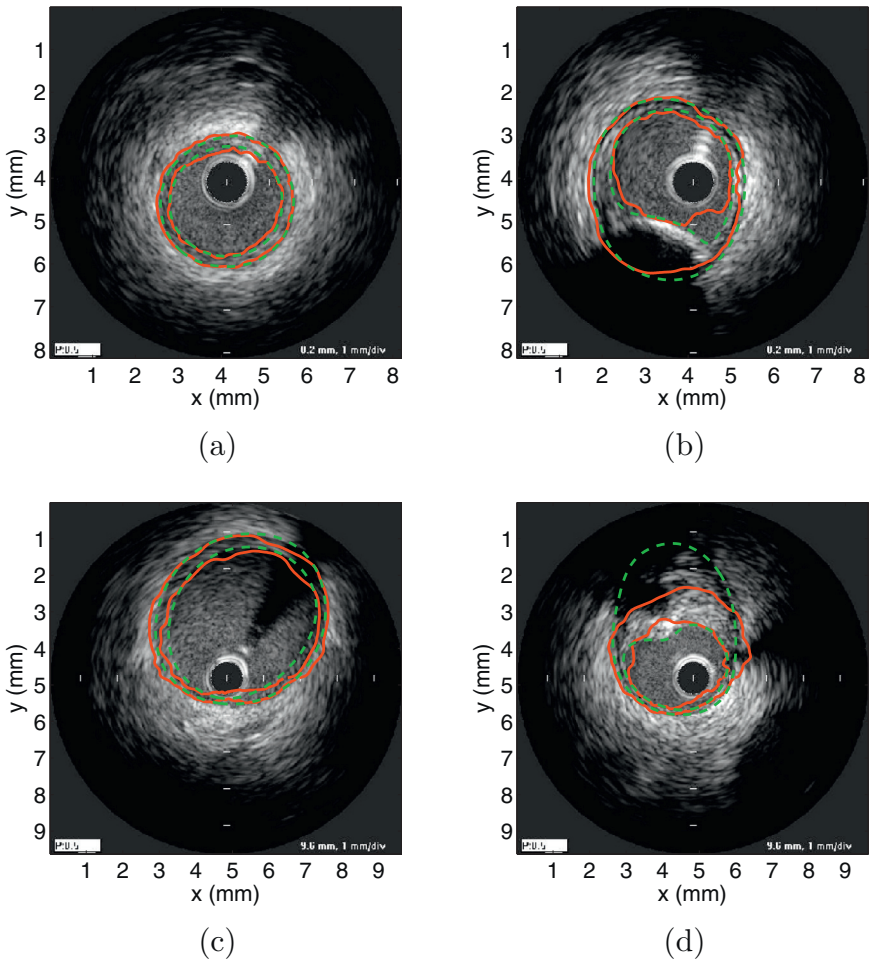

Fig. 5. First row: two frames from a dataset 2 sequence for which the combined Hausdorff distances (HD) for the lumen and EEM boundaries were the lowest (good concordance between algorithmic and manual segmentations). When averaged over the whole sequence, the HD for the lumen was 0.236 ± 0.113 mm, whereas it was 0.212 ± 0.071 mm for the EEM. Second row: two frames of another dataset 2 sequence for which combined HD for the lumen and EEM boundaries were highest (poor concordance between algorithmic and manual segmentations). When averaged over the whole sequence, the HD for the lumen was 0.617 ± 0.196 mm, whereas it was 0.620 ± 0.250 mm for the EEM. FMM segmentations (red full lines) compared with manual segmentations (green dashed lines). Frames with the best segmentation of each sequence (a) and (c). Frames with the worse segmentation of each sequence (b) and (d). (For interpretation of the references to color in this figure legend, the reader is referred to the web version of the article.)

of paired t-tests were all less than 10^{-3}. Note that the use of Rayleigh distributions in [19] were based on the hypothesis of fully developed speckle, which seemed valid for femoral IVUS imaging at 20 MHz. However, for the present study, it was preferable to adopt the gamma distributions. This behavior of the method [19] can be explained by the fact that at a higher frequency of 40 MHz, the hypothesis of fully developed speckle may not hold anymore since the number density of scatterers is then smaller due to a smaller resolution cell.

A further interesting comment can be made on our study. We have presented the first comparison of segmentations performed on "iLab" (dataset 1) versus "Galaxy II" (dataset 2) images. It is clear that technological developments by "Boston Scientific" allowed the acquisition of IVUS images of superior quality with their new platform generation, namely the "iLab" platform. [52] did notice the great variability in the texture of IVUS images acquired with the "Galaxy II" platform. Despite that fact, as shown in Table 2, the performance metrics were equivalent for "iLab" and "Galaxy" images for the EEM segmentation, although not for the lumen contours. The performance measures for the lumen were superior for "iLab" images, but nevertheless the Hausdorff distances were equivalent for both types of images. This can be explained by the fact that our segmentation algorithm is based on region and contour features of the IVUS images combining probability density functions of the vessel wall components and intensity gradients of the image gray levels. A better image quality (with a more uniform texture) makes the definition of image components easier, and hence also the segmentation.

Concerning the calibration of the parameters μ and λ in Eqs. (1) and (2), such that $E[1 + \{(1/N_v)\sum_{s\in v} P(s \in m|A_s)\} \times \{(1/N_w)\sum_{s\in w} P(s \in n|A_s)\}/\mu]$ and $E[1 + |\nabla G_\sigma * A_s|/\lambda]$ are equal to a same value c, we have tested the segmentation algorithm dataset 1 with an average value equal to $c = 8$ or $c = 12$, instead of 10. Then, Kruskal–Wallis one-way analysis of variance on ranks yielded no statistically significant differences on the various performance measures (in mm or mm^2) mentioned in Section 2.7.1 between the three groups of segmentations (i.e., x, using $c = 8$, 10 or 12). Thus, the performance of the proposed segmentation algorithm is robust to the choice of the average value c within the range 8–12. These tests were performed on dataset 1 since these images were acquired on a more recent platform than dataset 2.

We have compared the various dissimilarity measures (mean point-to-point distance MD, Hausdorff distance HD, error of

Author's personal copy

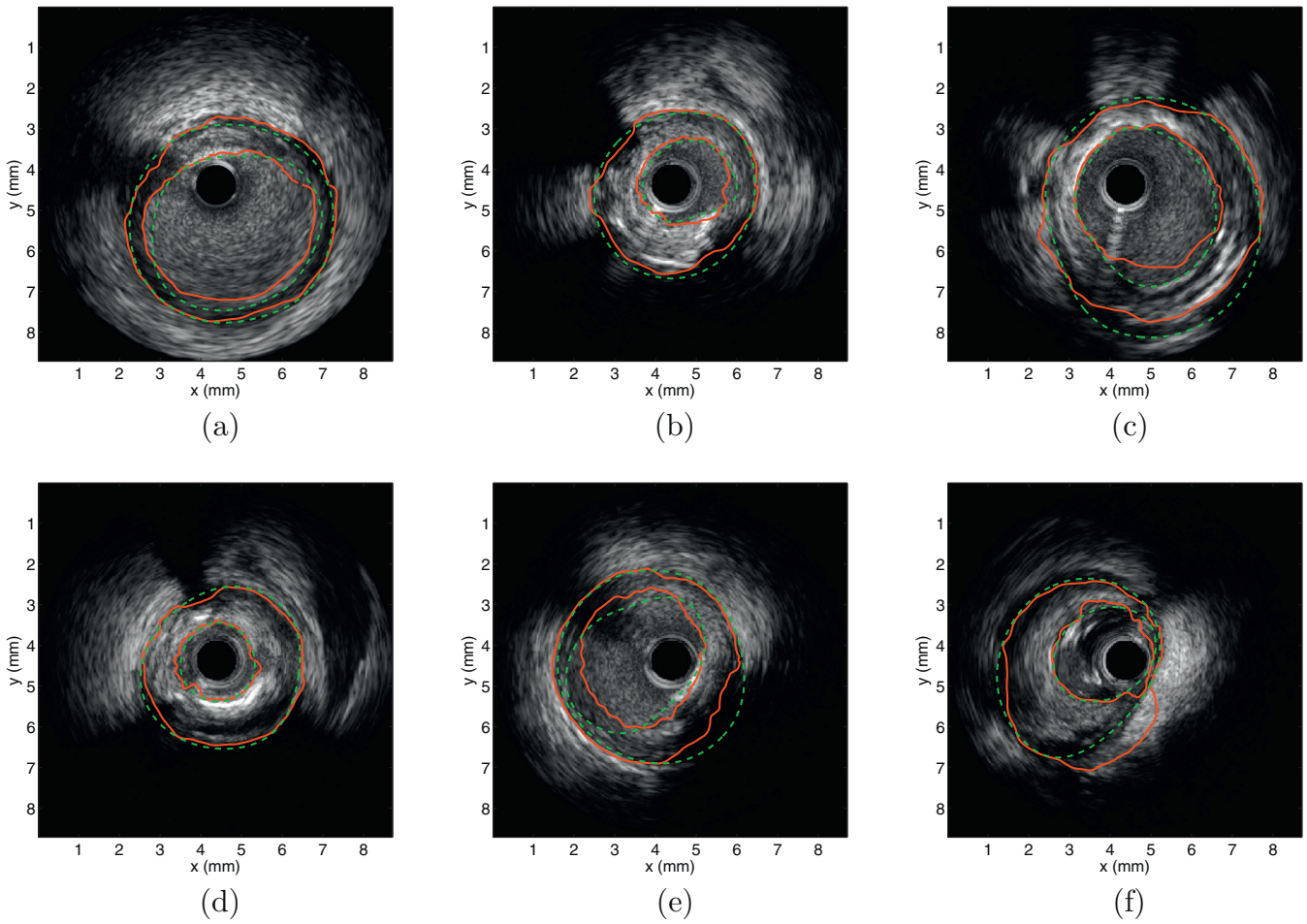

Fig. 6. Typical images from dataset 1 that presented difficulties in the manual segmentation. Cat. 1: no difficulty in the manual segmentation (a), the Hausdorff distance (HD) was 0.177 mm for the lumen, whereas it was 0.415 mm for the EEM. Cat. 2: dissection (b), the HD was 0.339 mm for the lumen, whereas it was 0.294 mm for the EEM. Cat. 4: stent (c), the HD was 0.479 mm for the lumen, whereas it was 0.535 mm for the EEM. Cat. 5: calcium and dissection (d), the HD was 0.184 mm for the lumen, whereas it was 0.182 mm for the EEM. Cat. 7: branching of the vessel and calcium (e), the HD was 0.563 mm for the lumen, whereas it was 0.541 mm for the EEM. Cat. 8: injection of a contrast agent (f), the HD was 0.284 mm for the lumen, whereas it was 0.662 mm for the EEM. FMM segmentations (red full lines) are compared with manual segmentations (green dashed lines). (For interpretation of the references to color in this figure legend, the reader is referred to the web version of the article.)

area EA) between the contours obtained from the random perturbations of the manual initializations of the L-views and the gold standard contours, on one hand, and these measures between the algorithmic segmentations based on the random perturbations and the same gold standards, on the other hand. For the MD between the EEM contours, the algorithmic segmentations improved significantly the random perturbations of the initializations for 0.2, 0.3 mm; for the EA, this was true for random perturbations of 0.3 mm. For the MD between the lumen contours, the improvement of the algorithmic segmentations on the random perturbations of the initializations was significantly better for 0.1, 0.2 and 0.3 mm. For the HD of the EEM and lumen contours, the random perturbations of the manual initializations were significantly better than the algorithmic segmentations based on those perturbations of the initializations. The other measures presented no significant differences except for the EA in percentage that was better for the initial contours. To illustrate further the improvement of the algorithmic segmentations on the MD measure, Fig. 7 presents the difference between the MD of the final computerized results and the initial contours versus the MD of the initial contours for the EEM and lumen boundaries, with or without ± 0.2 mm random perturbation of the manual initializations. From this figure, one can see the tendency of the algorithm to have improved the initial contours when these were further away from the gold-standards. Thus, the algorithm improved the initial contours the more so when the initial contours were less precise.

A last comment concerns the comparison between datasets 1 and 2 segmentations presented in Table 2, and the reproducibility study reported in Table 3. In all cases, the performance metrics in percentage were always better for the EEM than for the lumen. This fact could be interpreted as meaning that the lumen was more difficult to segment than the EEM. However, since the performance metrics are relative (i.e., expressed in percent) and since the diameter and the area of the lumen are always smaller than those of the EEM (because of the anatomy of the artery), it was expected to observe higher relative measures for the lumen. Indeed, in absolute units, i.e., mm for distances and mm^2 for areas, we have obtained an equivalent performance for the two boundaries with dataset 1, based on a *t*-test (but for the Hausdorff distances, the power of the test was below the desired power of 0, 800). On the other hand, for dataset 2, there was a significant difference between the mean-point-to-point and Hausdorff distances of the lumen and EEM boundaries. Again, this result can be explained by the lesser quality of the dataset 2 images compared to dataset 1.

Author's personal copy

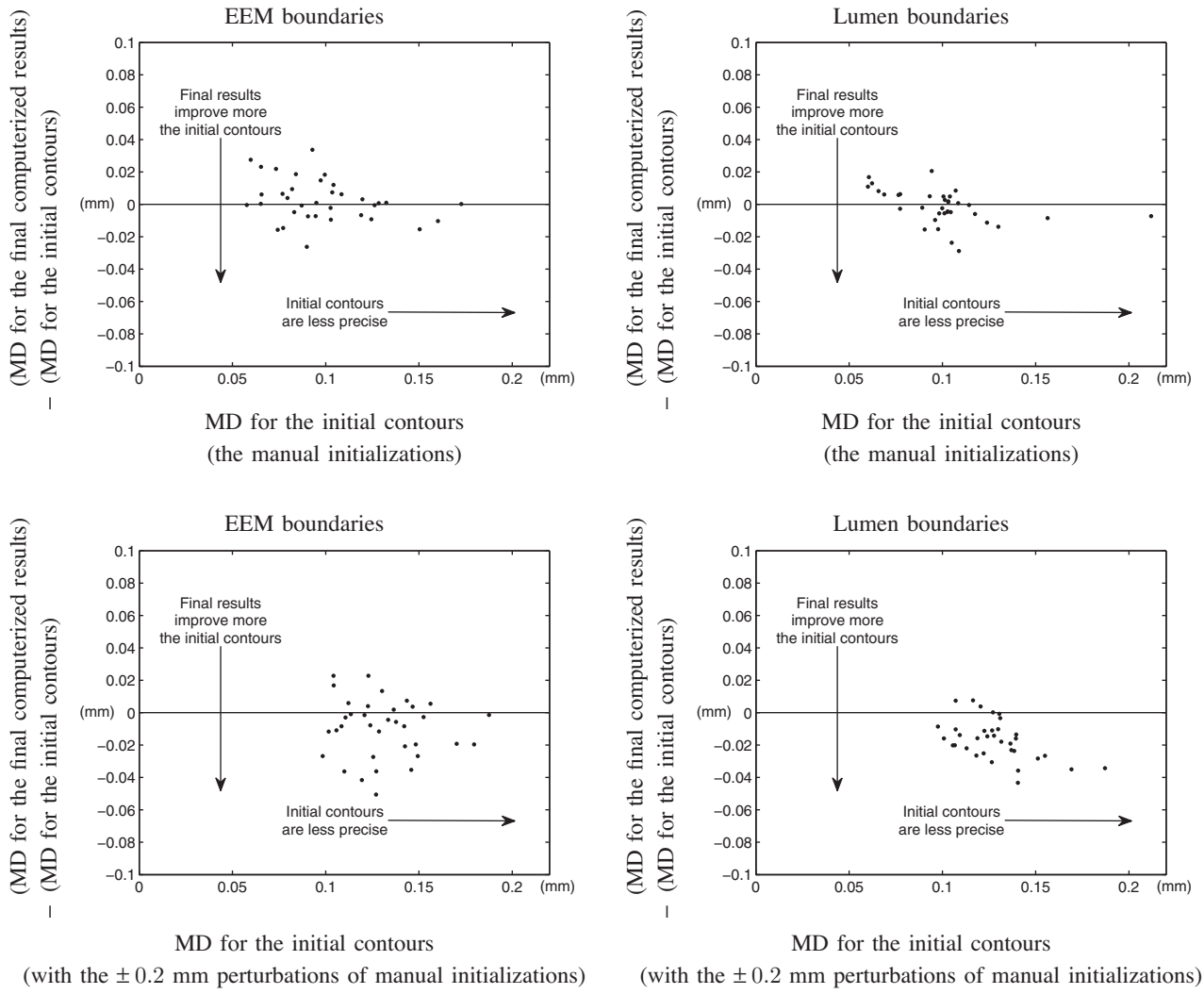

Fig. 7. Top: scatter plots of the difference between mean point-to-point distances (MD) of the final computerized results and initial contours versus the MD of the initial contours for the EEM and lumen boundaries, when the inital contours are the manual initializations. Bottom: corresponding scatter plots, when the initial contours are the ±0.2 mm random perturbations of the manual initializations. A negative value along the vertical axis indicates that the MD measure is better for the computerized results than for the initial contours. Thus, the algorithm improved the initial contours the more so when the initial contours were less precise.

5. Conclusion

This study showed with success, for the EEM as well as for the lumen, the good performance of the "fast-marching" algorithm based on the proposed region and contours-based speed functions, compared to other methods of the literature. Note that the PDFs were estimated on each sequence based on the initial contours. In this manner, the proposed method is adaptive to the appearance of the tissues due to various artifacts. An interesting avenue to pursue would be the development of a quantitative metric for the quality assessment of the FMM segmentations. According to Eq. (3), each boundary was defined by a speed function that depends on the contrast in PDF and intensity gradients of speckle inside and outside that boundary. One may calculate the mean speed of the boundary once stabilized to assess the value of that contrast as good (i.e., reliable segmentation), average (i.e., probable segmentation) and low (i.e., uncertain segmentation). With such a quality assessment for each IVUS image of a given sequence, one may decide to analyze only reliable and probable segmentations. This would allow analyzing, in clinical protocols, a much higher number of frames than it is currently the case, with manual segmentations.

Acknowledgments

This work was jointly supported by a grant from the Ministère du Développement Économique, Innovation et Exportation, Québec, Canada; and Boston Scientific, Freemont, CA, USA. Financial supports were also provided by the Natural Sciences and Engineering Research Council of Canada (grant #138570 - 06). Authors are acknowledging the contributions of Joanne Vincent, Colombe Roy and Ginette Grenier of the IVUS core laboratory of the Montreal Heart Institute for manually segmenting IVUS sequences, and of Boris Chayer of the Laboratory of Biorheology and Medical Ultrasonics (University of Montreal Hospital Research Center) for technical help in building the database.

References

[1] Nissen SE, Yock P. Intravascular ultrasound: novel pathophysiological insights and current clinical applications. Circulation 2001;103:604–16.
[2] Brusseau E, de Korte C, Mastik F, Schaar J, van der Steen A. Fully automatic luminal contour segmentation in intracoronary ultrasound imaging – a statistical approach. IEEE Trans Med Imaging 2004;23(5):554–66.
[3] Whale A, Lopez JJ, Olszewski ME, Vigmostad SC, Chandran KB, Rossen JD, et al. Plaque development, vessel curvature, and wall shear stress in coronary

Author's personal copy

arteries assessed by X-ray angiography and intravascular ultrasound. Med Image Anal 2006;10:615–31.
[4] Sanz-Requena R, Moratal D, García-Sánchez DR, Bodí V, Rieta JJ, Sanchis JM. Automatic segmentation and 3D reconstruction of intravascular ultrasound images for a fast preliminar evaluation of vessel pathologies. Comput Med Imaging Graph 2007;31:71–80.
[5] Unal G, Bucher S, Carlier S, Slabaugh G, Fang T, Tanaka K. Shape-driven segmentation of the arterial wall in intravascular ultrasound images. IEEE Trans Inf Technol Biomed 2008;12(3):861–74.
[6] Ciompi F, Pujol O, Fernández-Nofrerías E, Mauri J, Radeva PP. ECOC random fields for lumen segmentation in radial artery IVUS sequences. In: Yang G-Z, Hawkes D, Rueckert D, Noble A, Taylor C, editors. MICCAI 2009, Part II, LNCS 5762. Berlin Heidelberg: Springer-Verlag; 2009. p. 869–76.
[7] Gil D, Radeva P, Saludes J, Mauri J. Automatic segmentation of artery wall in coronary IVUS images: a probabilistic approach. Comput Cardiol 2000;27:687–90.
[8] Mendizabal-Ruiz EG, Rivera M, Kakadiaris IA. A probabilistic segmentation method for the identification of luminal borders in intravascular ultrasound images. In: Proc IEEE conf computer vision and pattern recognition. 2008. p. 1–8.
[9] Taki A, Najafi Z, Roodaki A, Setarehdan SK, Zoroofi RA, Konig A, et al. Automatic segmentation of calcified plaques and vessel borders in IVUS images. Int J CARDS 2008;3:347–54.
[10] Downe RW, Wahle A, Kovárník T, Skalická H, Lopez JJ, Horák J, et al. Segmentation of intravascular ultrasound images using graph search and a novel cost function. In: Proc of workshop on computer vision in intravascular and intracardiac imaging, MICCAI. 2008. p. 71–9.
[11] Bovenkamp E, Dijkstra J, Bosch J, Reiber J. User-agent cooperation in multiagent IVUS image segmentation. IEEE Trans Med Imaging 2009;28(1):94–105.
[12] Papadogiorgaki M, Mezaris V, Chatzizisis YS, Giannoglou GD, Kompatsiaris I. Image analysis techniques for automated IVUS contour detection. Ultrasound Med Biol 2008;34(9):1482–98.
[13] Katouzian A, Angelini ED, Sturm B, Laine AF. Automatic detection of luminal borders in ivus images by magnitude-phase histograms of complex brushlet coefficients. In: Proc of 32nd annual international conference of the IEEE EMBS. 2010. p. 3073–6.
[14] Moraes M, Furuie S. Automatic coronary wall segmentation in intravascular ultrasound images using binary morphological reconstruction. Ultrasound Med Biol 2011;37(9):1486–99.
[15] Mendizabal-Ruiz EG, Rivera M, Kakadiaris IA. Segmentation of the luminal border in intravascular ultrasound B-mode images using a probabilistic approach. Med Image Anal 2013;17(6):649–70.
[16] Ciompi F, Pujol O, Gatta C, Alberti M, Balocco S, Carrillo X, et al. HoliMAb: a holistic approach for media-adventitia border detection in intravascular ultrasound. Med Image Anal 2012;16:1085–100.
[17] Sun Z, Liu C. A parallel method for segmenting intravascular ultrasound image sequence. Appl Mech Mater 2011;130-134:2051–5.
[18] Roy Cardinal M-H, Meunier J, Soulez G, Maurice RL, Therasse É, Cloutier G. Intravascular ultrasound image segmentation: a three-dimensional fast-marching method based on gray level distributions. IEEE Trans Med Imaging 2006;25(5):590–601.
[19] Roy Cardinal M-H, Soulez G, Tardif JC, Meunier J, Cloutier G. Fast-marching segmentation of three-dimensional intravascular ultrasound images: a pre- and post-intervention study. Med Phys 2010;37(7):3633–47.
[20] Destrempes F, Cloutier G. A critical review and uniformized representation of statistical distributions modeling the ultrasound echo envelope. Ultrasound Med Biol 2010;36(7):1037–51.
[21] Dutt V, Greenleaf JF. Ultrasound echo envelope analysis using a homodyned *k* distribution signal model. Ultrason Imaging 1994;16:265–87.
[22] Wagner RF, Smith SW, Sandrick JM, Lopez H. Statistics of speckle in ultrasound B-scans. IEEE Trans Sonics Ultrasonic 1983;30(3):156–63.
[23] Berry C, L'Allier PL, Lespérance J, Lévesque S, Ibrahim R, Tardif JC. Comparison of intravascular ultrasound and quantitative coronary angiography for the assessment of coronary artery disease progression. Circulation 2007;115:1851–7.
[24] Sethian JA. A fast marching level set method for monotonically advancing fronts. Proc Natl Acad Sci 1996;93:1591–5.
[25] Sifakis E, Garcia C, Tziritas G. Bayesian level sets for image segmentation. J Visual Commun Image Represent 2002;13:44–64.
[26] Will S, Hermes L, Buhmann JM. On learning texture edge detectors. In: IEEE proc conf image proc. 2000. p. 877–80.
[27] Shankar PM. A general statistical model for ultrasonic scattering from tissues. IEEE Trans Ultrasonic Ferroelectr Freq Control 2000;47(3):727–36.
[28] Prager RW, Gee AH, Treece GM, Berman LH. Decompression and speckle detection for ultrasound images using the homodyned *k*-distribution. Pattern Recogn Lett 2003;24(4–5):705–13.
[29] Tao Z, Tagare HD. Evaluation of four probability distribution models for speckle in clinical cardiac ultrasound images. IEEE Trans Med Imaging 2006;25(11):1483–91.
[30] Nillesen MM, Lopata RGP, Gerrits IH, Kapusta L, Thussen JM, de Korte CL. Modeling envelope statistics of blood and myocardium for segmentation of echocardiographic images. Ultrasound Med Biol 2008;34(4):674–80.
[31] Dempster A, Laird N, Rubin D. Maximum likelihood from incomplete data via the EM algorithm. J R Stat Soc (Ser B) 1977;39:1–38.
[32] Destrempes F, Meunier J, Giroux M-F, Soulez G, Cloutier G. Segmentation in ultrasonic B-mode images of healthy carotid arteries using mixtures of Nakagami distributions and stochastic optimization. IEEE Trans Med Imaging 2009;28(2):215–29.
[33] Destrempes F, Meunier J, Giroux M-F, Soulez G, Cloutier G. Segmentation of plaques in sequences of ultrasonic B-mode images of carotid arteries based on motion estimation and a Bayesian model. IEEE Trans Biomed Eng 2011;58(8):2202–11.
[34] Huttenlocher DP, Klanderman GA, Rucklidge WJ. Comparing images using the hausdorff distance. IEEE Trans Pattern Anal Mach Intell 1993;15:850–63.
[35] Kovalski G, Beyar R, Shofti R, Azhari H. Three-dimensional automatic quantitative analysis of intravascular ultrasound images. Ultrasound Med Biol 2000;26(4):527–37.
[36] Guerrero J, Salcudean SE, McEwen JA, Masri BA, Nicolaou S. Real-time vessel segmentation and tracking for ultrasound imaging applications. IEEE Trans Med Imaging 2007;26(8):1079–90.
[37] Li W. Image and signal processing in intravascular ultrasound. PhD Thesis. The Netherlands: Erasmus University Rotterdam; 1997. 204 p.
[38] Takagi A, Hibi K, Zhang X, Teo T, Bonneau H, Yock P, et al. Automated contour detection for high-frequency intravascular ultrasound imaging: a technique with blood noise reduction for edge enhancement. Ultrasound Med Biol 2000;26(6):1033–41.
[39] Bovenkamp EGP, Dijkstra J, Bosch JG, Reiber JH. Multi-agent segmentation of IVUS images. Pattern Recogn 2004;37(4):647–63.
[40] von Birgelen C, Mario C, Li W, Schuurbiers J, Slager C, de Feyter P, et al. Morphometric analysis in three-dimensional intracoronary ultrasound: an in vitro and in vivo study using a novel system for the contour detection of lumen and plaque. Am Heart J 1996;132(2):516–27.
[41] Sonka M, Zhang X, Siebes M, Bissing MS, DeJong SC, Collins SM, et al. Segmentation of intravascular ultrasound images: a knowledge-based approach. IEEE Trans Med Imaging 1995;14(4):719–32.
[42] Mojsilovic A, Popovic M, Amodaj N, Babic R, Ostojic M. Automatic segmentation of intravascular ultrasound images: a texture-based approach. Ann Biomed Eng 1997;25:1059–71.
[43] Zhang X, McKay CR, Sonka M. Tissue characterization in intravascular ultrasound images. IEEE Trans Med Imaging 1998;17(6):889–99.
[44] Haas C, Ermert H, Holt S, Grewe P, Machraoui A, Barmeyer J. Segmentation of 3D intravascular ultrasound images based on a random field model. Ultrasound Med Biol 2000;26(2):297–306.
[45] Klingensmith JD, Shekhar R, Vince DG. Evaluation of three-dimensional segmentation algorithms for the identification of luminal and medial-adventitial borders in intravascular ultrasound images. IEEE Trans Med Imaging 2000;19(10):996–1011.
[46] Plissiti ME, Fotiadis DI, Michalis LK, Bozios GE. An automated method for lumen and media-adventitia border detection in a sequence of IVUS frames. IEEE Trans Inf Technol Biomed 2004;8(2):131–41.
[47] Koning G, Dijkstra J, vonBirgelen C, Tuinenburg JC, Brunette J, Tardif J-C, et al. Advanced contour detection for three-dimensional intracoronary ultrasound: a validation – in vitro and in vivo. The International Journal of Cardiovascular Imaging 2002;18:235–48.
[48] Gil D, Hernàndez A, Rodriguez O, Mauri J, Radeva P. Statistical strategy for anisotropic adventitia modelling in IVUS. IEEE Trans Med Imaging 2006;25(6):768–78.
[49] Giannoglou GD, Chatzizisis YS, Koutkias V, Kompatsiaris I, Papadogiorgaki M, Mezaris V, et al. A novel active contour model for fully automated segmentation of intravascular ultrasound images: in vivo validation in human coronary arteries. Comput Biol Med 2007;37:1292–302.
[50] Katouzian A, Angelini E, Carlier S, Suri J, Navab N, Laine A. A state of the art review on segmentation algorithms in intravascular ultrasound (IVUS) images. IEEE Trans Inf Technol Biomed 2012;16(5):823–34.
[51] Balocco S, Gatta C, Ciompi F, Wahle A, Radeva P, Carlier S, et al. Standardized evaluation methodology and reference database for evaluating IVUS image segmentation. Comp Med Imag Graph 2014;38(2):70–90.
[52] Hernàndez A, Radeva P, Tovar A, Gil D. Vessel structures alignment by spectral analysis of IVUS sequences. In: Proc of first international workshop on computer vision for intravascular and intracardiac imaging, MICCAI. 2006. p. 29–36.